Journal of Catalysis 264 (2009) 163–174

Contents lists available at ScienceDirect

Journal of Catalysis

journal homepage: www.elsevier.com/locate/jcat

Binuclear μ-hydroxo-bridged iron clusters derived from surface organometallic chemistry of ferrocene in cavities of HY zeolite: Local structure, bound sites, and catalytic reactivity

Jinlin Long, Xuxu Wang *, Zhengxin Ding, Zizhong Zhang, Huaxiang Lin, Wenxin Dai, Xianzhi Fu *

Research Institute of Photocatalysis, State Key Laboratory Breeding Base of Photocatalysis, Fuzhou University, Fuzhou 350002, China

ARTICLE INFO

Article history:
Received 19 January 2009
Revised 30 March 2009
Accepted 1 April 2009
Available online 6 May 2009

Keywords:
Iron
Zeolite
Phenol hydroxylation
X-ray absorption fine structure spectroscopy
Catalysis

ABSTRACT

Binuclear iron clusters were constructed successfully in cavities of HY Zeolite by surface organometallic chemistry (SOMC) of ferrocene. UV–visible diffuse reflection (UV–vis DRS), X-ray absorption fine structure (XAFS), electron paramagnetic resonance (EPR), and infrared (IR) spectroscopies were used to characterize the structure of the formed binuclear iron clusters. The results show that the majority is presented as binuclear μ-hydroxo-bridged iron clusters consisting of a [Fe^{III}–(μ-OH)–Fe^{III}] core, which is anchored on the zeolite framework by the bonding of Fe atom and bridging O sites that lie in a plane of a 12-membered ring connecting the supercages. These binuclear iron clusters show better catalytic reactivity towards phenol hydroxylation than large iron oxide clusters. Iron oxide as active component was found to represent a nuclearity-related catalytic behavior for phenol hydroxylation. The decrease in nuclearity of iron oxides from nanoparticles to binuclear iron clusters leads to the increase in conversion and to the drastic decrease in induction time.

1. Introduction

Metal or metal oxide supported zeolite or other high-surface-area inorganic material is a class of the most widely used catalysts [1–3]. On such a catalyst, the metals or metal oxides are catalytically active components. Depending on the preparation method, they are often highly dispersed on the surface of the support as clusters or as mononuclear complexes. The clusters consisting of a few metal atoms differ structurally from the bulk counterparts and often offer new catalytic functions and enhanced catalytic activity dependent on size of the clusters. Insight into the inherent relationship between the catalytic function and the size and structure of the cluster has been a focus of attention in the catalysis community.

Zeolite-supported iron is a very typical example of the catalysts. It has received considerable attention due to its catalytic potential in a number of environmentally benign catalytic processes, including direct N_2O decomposition [4–6], selective catalytic reduction of NO_x [7–9], one-step hydroxylation of benzene to phenol with N_2O [10–12], propylene epoxidation by N_2O [13], and hydroxylation of phenol with H_2O_2 [14–16]. However, to date the inherent relationship between the catalytic function and the active iron sites of these iron-catalyzed reactions has been uncertain. A major problem with Fe-zeolites prepared by post-synthetic ion exchange in the solid or liquid phase and chemical vapor decomposition (CVD) of $FeCl_3$ as well as isomorphous substitution, particularly at high Fe content, is a tendency of the Fe species to cluster into aggregates. This leads to a very heterogeneous distribution of iron species with different nuclearity (from the isolated iron cations to oxide clusters, passing through dimers and small oligomers in ion exchange positions) in these materials [17–19], which hinders a definitive identification of active sites, though much of the work has been devoted to characterize the active states of iron with a multitude of physicochemical techniques [20–22].

Of the active iron sites within zeolites, two kinds of Fe-oxo species were extensively studied. One is binuclear oxygen-bridged Fe sites derived from EXAFS studies [23], which have been claimed to be active sites for N_2O decomposition (α-site) [10] and hydrocarbon-SCR [19,24]. On the other hand, Jia et al. [25] and Yuranvo et al. [26] proposed that mononuclear iron is responsible for benzene hydroxylation. Sun et al. [27] proposed that hydroxylation of benzene and N_2O decomposition do not take place at the same active sites. Oligonuclear, perhaps binuclear, iron sites appear most favorable for nitrous oxide decomposition, whereas the mononuclear iron sites are active for benzene hydroxylation to phenol. The debate concerning the nuclearity of catalytic sites (mono- or dinuclear) is still alive, whereas it is generally accepted that extra framework oxygen-bridged diferric species are involved in the formation of so-called "α-Oxygen" sites first described by Panov [10], which can selectively oxidize benzene to phenol at room temperature. The unique structure of the oxygen-bridged diferric

* Corresponding authors. Fax: +86 591 83738608.
E-mail addresses: xwang@fzu.edu.cn (X. Wang), xzfu@fzu.edu.cn (X. Fu).

0021-9517/$ - see front matter © 2009 Elsevier Inc. All rights reserved.
doi:10.1016/j.jcat.2009.04.002

complexes, representing structural mimics of the active center of iron-containing enzymes, such as cytochrome P450 and methane monooxygenase (MMO) [23,28], has prompted the design and development of new bio-inspired di-iron catalysts for hydroxylation and epoxidation.

Y Zeolite is a useful scaffold for molecular engineering of the dinuclear iron active sites owing to its spatial confinement of the cavities, which can result in an unusual geometry of the metal site. In the previous work, we successfully constructed mononuclear cyclopentadiene–iron and FeO_4 species with uniform distribution in the supercages of Y zeolite by use of surface organometallic chemistry of ferrocene [29,30]. A logical extension of our work on grafted iron species is on binuclear iron clusters. The main objective of the present study was to explore a novel route to the synthesis of surface-bound dinuclear iron clusters in the cavities of HY zeolite and thus attempt to gain deeper insight into the nature of iron-catalyzed reaction.

In the present work, we studied in detail the structure and catalytic reactivity of zeolite-bound iron species with high iron content, obtained by controlling the grafted amount of ferrocene, by X-ray absorption fine structure (XAFS) spectroscopy in combination with electron paramagnetic resonance (EPR), in situ infrared (IR) and UV–visible diffuse reflection (UV–vis DRS) spectroscopies. Phenol hydroxylation was used as a model reaction to examine the catalytic reactivity of these iron species. The characterization results revealed that the majority of iron is presented as hydroxo-bridged binuclear iron clusters in Fe-grafted HY zeolite when the grafted iron content is controlled in the range of 2.1 to 8.2 wt.%. The hydroxo-bridged dinuclear iron clusters present a higher phenol conversion and a shorter induction period than α-Fe_2O_3 nanoparticles and Fe-impregnated HY and Fe-impregnated NaY catalysts. The activity results show that the iron oxide catalysts exhibit the nuclearity-related catalytic behavior for phenol hydroxylation. Fe sites with low nuclearity should be responsible for the catalytic behavior.

2. Experimental

2.1. Materials

The NH_4Y and NaY zeolites were purchased from Aldrich. Its SiO_2/Al_2O_3 ratio was 5.1. Ferrocene ($C_{10}H_{10}Fe$, 98%) was purchased by Acros and purified by sublimation under vacuum prior to use. $FeCl_3 \cdot 6H_2O$ and NaOH were purchased by Guangzhou Chemical Reagent Corporation, China. The NH_4Y zeolite was first treated at 793 K for 20 h under flowing oxygen in order to completely transform it into H-type Y zeolite.

2.2. Preparation of catalysts

The samples denoted as Fe/HY-G*x* (*x*: iron content) were prepared by surface organometallic chemistry of ferrocene (SOMC method). The preparation was performed in a glassware equipment connected to a vacuum line. NH_4Y zeolite (ca. 1.0 g) was first treated at 673 K for 24 h under flowing oxygen in order to completely transform it into H-type Y zeolite, accompanied by treatment under vacuum (4×10^{-2} Pa) at 673 K for 3 h after cooling to room temperature, then certain amount of ferrocene was introduced onto the zeolite by sublimation. The system was then kept at 423 K for ca. 50 h in order to insure a complete reaction. More experimental details are described in Ref. [29,30]. The resulting solid was treated at 773 K for 4 h in oxygen and subsequently exposed to air. The samples denoted as Fe/HY-Ix (x: iron content) were prepared by wetness impregnation (WI) method. HY or NaY zeolite (2 g) was added to an aqueous solution of $FeCl_3$ followed by heating at 353 K with stirring for 2 h. The solid was recovered and dried at 393 K for 12 h, and then calcined at 773 K for 4 h in air. α-Fe_2O_3 sample was prepared by a two-step procedure. First, 100 ml of 3 M NaOH was added to 400 ml of 0.2 M $FeCl_3$ aqueous solution under magnetic stirring at room temperature, a precipitate was instantly formed and separated by centrifugation and washed with water several times and dried in air. Then, the obtained solid was sintered in the electric muffle furnace at 573 K for 2 h and checked by XRD.

2.3. Catalyst characterization

Inductively coupled plasma (ICP) atomic emission spectrometry was used for the determination of Fe content in the samples. UV–vis spectroscopic measurements (DRS) were recorded on a Varian Carry 500 UV/VIS/NIR spectrometer. The spectra were corrected at 200 to 800 nm referenced to $BaSO_4$ and were transformed into the Kubelka–Munk function, $F(R\infty)$.

The IR experiments were carried out on a Nicolet 670 FTIR spectrometer with a DTGS detector. In situ IR spectra of NO adsorption on ca. 20 mg of self-supporting wafer were recorded at the given partial pressures of NO with a homemade in situ IR cell equipped with CaF_2 transparent windows at room temperature. In all experiments, the IR spectrum collected before gas dosage was used as background. All reported spectra of NO adsorption are background subtracted. Each spectrum consists of 32 scans taken at 4 cm^{-1} resolution. Typically, the sample was first pretreated under dynamic vacuum at 673 K for 3 h, and then cooled to room temperature in vacuum (pressure lower than 10^{-6} mbar) prior to contacting with NO (purity 99.9%).

The X-ray absorption experiments were performed at the XAFS station (Beamline 4W1B) of the Beijing Synchrotron Irradiation Facility (BSRF) with stored electron energy of 2.2 GeV and ring currents between 160 and 250 mA. Data were collected in a transmission mode at room temperature with a sampling step of ~1.0 eV for XANES and ~3.0 eV for extended X-ray absorption fine structure (EXAFS). In all cases, the irradiation was monochromatized using a Si(3 1 1) double-crystal monochromator. The intensities of the incident and transmitted beams were monitored using two N_2 and 50% argon-doped N_2 filled ionization chambers, respectively. Energies of samples were calibrated using a Fe metal foil standard, assigning the starting point of K-edge to 7111.2 eV. The energy resolution is 0.3 eV.

The data treatment was carried out using the software package WinXAS2.0. For background subtraction and X-ray absorption near edge structure (XANES) normalization a linear polynomial was fitted to the pre-edge region and a third-order polynomial to the post-edge region. The radial structural function (RSF) FT $[k^3x(k)]$ was obtained by Fourier transformation of the k^3-weighted experimental function $(x(k))$ $(I(k) - I_0(k))/I_0(k)$ multiplied by a Gauss window in the range 2.4 to 13.9 $Å^{-1}$. The Fourier-filtered data were fitted in *R*-space in the range 1 to 4 Å for α-Fe_2O_3 and in the range 1 to 3 Å for other samples. To obtain the structural parameters including interatomic distances (*R*), coordination numbers (CN), Debye–Waller factors ($\Delta\sigma^2$), and edge energy shifts (ΔE_0), phase shifts and backscattering amplitudes extracted from a reference material α-Fe_2O_3 (Fe–O) were used to fit the EXAFS data. The validity of a fit was checked by the fitting of k^3-weighted spectra in *k*-space. The quality of a fit was estimated from the values of the variances of the imaginary and absolute parts of the FT.

Electron paramagnetic resonance spectra were recorded on a Bruker ELEXSYS E300 spectrometer at liquid nitrogen temperature. The spectrometer was operated at X-band frequency, with a microwave power of 0.635 mW and 100 kHz field modulation. The Bruker ELEXSYS E300 software and the special Bruker program WIN-EPR were used for the treatment of (baseline correction, noise reduction and double integration) the recorded spectra.

2.4. Activity test of the catalysts

Phenol hydroxylation was carried out in a 50 mL three-necked glass round-bottomed flask fitted with a condenser. In a standard reaction, ~1.0 g of phenol and ~0.05 g of catalyst were firstly added to 20 mL of deionized water in the reactor. Hydrogen peroxide (H_2O_2, 30% aqueous solution) was added through a transfer pipet to the magnetically stirred phenol solution containing catalyst at 320 K (phenol: H_2O_2 = 1:1, molar ratio, stirring rate: 1000 r min^{-1}). The reaction was monitored by periodically sampling with a syringe and analyzed on HPLC Waters 2487 equipped with a Merck C8 column. The products were separated on the column using a methanol/water mixture (60/40, volume ratio) as the mobile phase at a flow rate of 0.6 mL/min with dual wavelength UV detection at 245 and 271 nm. The identification and quantification of reactant and products were performed using standard compounds (phenol, hydroquinone, and catechol).

3. Results

3.1. Bound sites of iron atom

To gain information on the location of iron atoms in cavities of Y zeolite, we in situ monitor the reaction of ferrocene with acidic hydroxyl groups in the supercages of HY zeolite with FT-IR spectroscopy, as shown in Fig. 1. After dehydration at 673 K for 3 h in vacuum, HY zeolite (ca. 30 mg disc with a diameter of 18 mm) exhibits three distinct hydroxyl bands at 3740, 3640, and 3550 cm^{-1} in the IR spectrum (Fig. 1a). The bands at 3740, 3640, and 3550 cm^{-1} are assigned unambiguously to the isolated silanol groups, the acidic O_1H groups that lie approximately in a plane of a 12-membered ring connecting the supercages of the structure, and the acidic O_2H groups in the plane of the six-membered ring of the sodalite units, respectively [31]. The sublimation of excessive ferrocene causes the disappearance of a majority of the acidic O_1H band in the supercages, and the less intense acidic O_2H band in the sodalite units (Fig. 1b). Simultaneously, a broad and strong band, indicating hydrogen bonding between the O_1H and O_2H groups and the adsorbent ferrocene, occurs at 3300 cm^{-1}. After heating at 423 K for 17 h and evacuating at the same temperature for 6 h, the hydrogen bonding band at 3300 cm^{-1} and the acidic O_1H band at 3640 cm^{-1} disappear completely along with the emergence of C–H stretching band at the range of 2800–3100 cm^{-1} (Fig. 1c), indicating that the O_1H groups are consumed completely. The moiety of ferrocene is anchored on the framework O_1 sites [29]. This heating at such a temperature simultaneously results in the significant decrease in intensity of the O_2H band at 3550 cm^{-1}, indicating that the grafting reaction can take place at the framework O_2 sites in the sodalite cages when ferrocene loading is excessive, leading to the cyclopentadiene–iron moiety bound on the framework O_2 sites. After removal of surface organic ligands by in situ calcination at 773 K in oxygen flowing atmosphere, IR spectrum (Fig. 1d) displays a silanol band at 3740 cm^{-1} and a non-acidic or inaccessible hydroxyl band at 3633 cm^{-1} [32] as well as the unreacted O_2H band at 3560 cm^{-1}. The complete disappearance of the O_1H groups demonstrates that Fe is bonded to O_1 atoms framework to form Fe–O_1 species by replacing protons in the supercages. In the case of excessive ferrocene, a fraction of Fe can be anchored to O_2 atoms in the sodalite cages to produce Fe–O_2 species.

We used the SOMC method to prepare three Fe-grafted HY zeolite samples, and subsequently these three samples were exposed to air. Element analysis shows that these three samples contain 2.1, 5.1, and 8.2 wt.%, respectively, of iron content (denoted, respectively, as Fe/HY-G2.1, -G5.1 and, -G8.2). After outgassed in dynamic vacuum at 673 K for 3 h, these three Fe/HY-G*x* samples (Fig. 2a to c) represent different IR spectra in the hydroxyl region compared to the sample unexposed to air (Fig. 1d). Three new absorption bands occur at 3687, 3668, and 3596 cm^{-1}. These two bands at 3668 and 3596 cm^{-1}, which are observed for dealuminated HY zeolite, are generally attributed to the hydroxyl groups associated with extraframework aluminum (ex Al-OH) and the acidic OH groups in the sodalite cages, respectively [33]. However, for the band at 3687 cm^{-1}, Nobukawa et al. observed a similar absorption band at 3683 cm^{-1} on Fe ion-exchanged BEA zeolite catalysts and attributed the band to Fe-OH [34]. Based on the similar bands on Fe-containing zeolites and FeOOH [35], we tentatively ascribe the band at 3687 cm^{-1} to Fe^{III}-OH.

3.2. UV–vis spectroscopy

The coordination environment of iron species was characterized using UV–vis diffuse reflectance spectroscopy as displayed in Fig. 3. The UV–vis absorption spectra of Fe/HY-I5.0 and Fe/NaY-I5.0, which were used as a reference, exhibit strong absorbance in 200

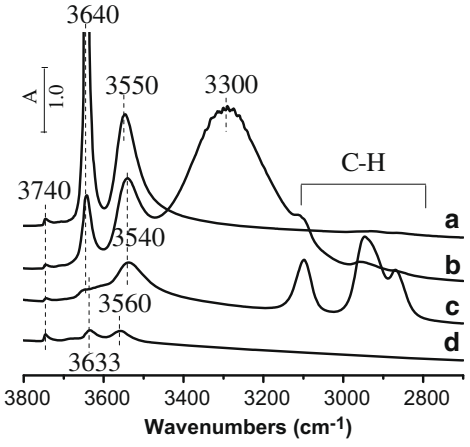

Fig. 1. In situ FTIR spectra in the region of 2700–3800 cm^{-1} of HY zeolite before and after grafting of Cp_2Fe: (a) HY zeolite dehydrated at 673 K in vacuum; (b) after adsorption of ferrocene at room temperature; (c) after heating at 423 K for 17 h and elimination of physisorbed species at 423 K in vacuum; (d) after in situ calcination at 773 K for 4 h in flowing oxygen and dehydration at 673 K in vacuum.

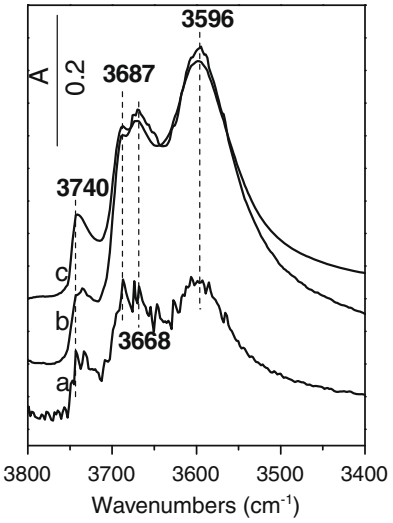

Fig. 2. FTIR spectra in the region of 3400–3800 cm^{-1} of (a) Fe/HY-G8.2 dehydrated at 673 K in vacuum, (b) Fe/HY-G2.1 dehydrated at 673 K in vacuum, and (c) Fe/HY-G5.1 dehydrated at 673 K in vacuum.

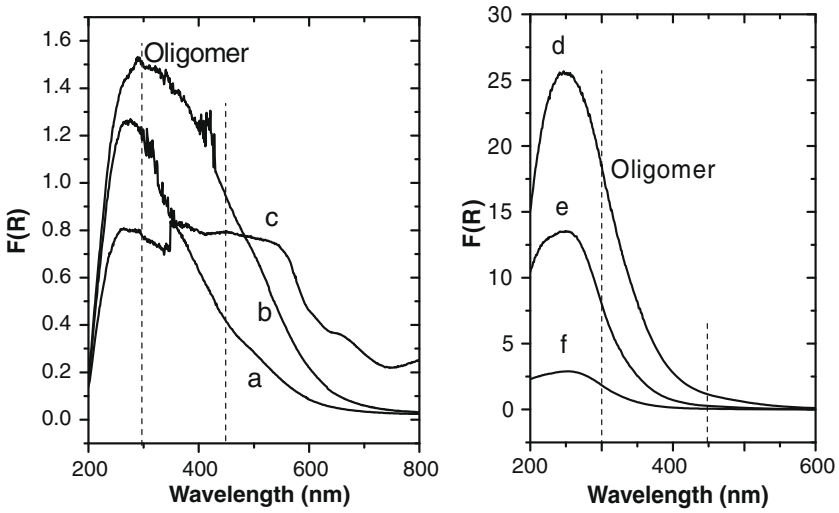

Fig. 3. UV–vis DRS spectra of (a) Fe/HY-I5.0, (b) Fe/NaY-I5.0, (c) Nano-α-Fe_2O_3, (d) Fe/HY-G8.2, (e) Fe/HY-G5.1, and (f) Fe/HY-G2.1.

to 800 nm (Fig. 3a to c), revealing the existence of complicated iron species in these two Fe-zeolite samples prepared by WI method. A stronger absorption band attributed usually to Fe_2O_3 nanoparticles occurs at ca. 500 nm for the Fe/NaY-I5.0 sample (Fig. 3b), indicating that Fe/NaY-I5.0 contains more Fe_2O_3 nanoparticles under the same iron content. However, no absorption band above 450 nm is observed in UV–vis spectra for the three Fe/HY-G*x* samples (Fig. 3d to f), suggesting that the three Fe/HY-G*x* samples prepared by SOMC method are free of iron oxide species comparable with nanoscale Fe_2O_3. A strong and broad absorption feature centered at ca. 260 nm and a shoulder peak at 215 nm dominates the UV–vis spectra of the three Fe/HY-G*x* samples. The tail absorption in the range of 300 to 450, which decreases in intensity with decreasing iron content, indicates the presence of a fraction of oligonuclear iron clusters in the Fe/HY-G*x* samples [20]. The bands below 300 nm are frequently attributed to the oxygen-to-iron charge transfer of isolated iron species either tetrahedrally or octahedrally coordinated [21], but a recent detailed analysis [36] revealed that iron dimers also show UV–vis absorptions below 300 nm. Thus, the presence of these two bands at ca. 215 and 260 nm does not constitute sufficient evidence of either isolated iron species or binuclear iron clusters present in the Fe/HY-G*x* samples, unless there are further evidences from other characterizations such as XAFS, EPR, and IR techniques.

3.3. XANES and EXAFS spectroscopy

The local structure of iron species was characterized by X-ray absorption spectroscopy. Fe K-edge XAFS data were obtained for the three Fe/HY-G*x* samples. The XAFS data of α-Fe_2O_3 were used as a reference. The normalized XANES spectra collected at the Fe K-edge for the Fe/HY-G*x* samples are shown in Fig. 4. Reliable information can be drawn from the centroid and total integrated intensity of the pre-edge peak A, from the edge position, and from the existence of multiple scattering features beyond the edge, which are labeled D and E. The edge positions and pre-edge centriods of all samples are consistent with that of the reference α-Fe_2O_3, which indicates that iron is predominant in the +3 oxidation state.

The pre-edge absorption in Fe K-edge XANES spectra originates from a 1 s → 3 d transition, which is forbidden in octahedral coordination but occurs in coordinations without inversion center (distorted octahedral, tetrahedral). As seen in Fig. 4B, these Fe/HY-G*x* samples represent a more intense and narrower pre-edge feature A than that of α-Fe_2O_3 (where iron is six-coordinated). Whereas the intensity of the pre-edge feature is lower than that of the four-coordinated iron in ferrisilicate reported in the previous work [37], indicating that the CN of iron in the Fe/HY-G*x* samples should be between four and six. This will be further validated by the EXAFS fit results given below. The position of the absorption maximum C for these Fe/HY-G*x* samples, which corresponds to transitions to unfilled 4p states, differs significantly from that of the hematite reference. It is shifted by ca. 2.0 eV to lower energies compared to α-Fe_2O_3, which is originated from the hybridization of the iron 4p and partly 3d atomic orbitals. The difference between the Fe/HY-G*x* samples and α-Fe_2O_3 can also be seen in the edge shape and post-edge region (B, C, D, and E).

k^3-weighted EXAFS Fourier transformation spectra of α-Fe_2O_3 and Fe/HY-G*x* samples are shown in Fig. 6. The feature at ca. 1.6 Å is attributed to Fe–O backscattering in the first coordination sphere. Two peaks at 2.4 to 3.4 Å observed for α-Fe_2O_3 originate from two different kinds of Fe–O–Fe, and the wide scattering at ca. 4.0 Å is assignable to large oxide particles. In contrast to α-Fe_2O_3, all Fe/HY-G*x* samples show two distinct peaks at 1.6 and 2.8 Å (without phase correction). No scattering feature is observed beyond 3.5 Å, indicating the absence of large iron oxide particles. The appearance of this radial structural function (RSF) in *R* space is very similar to that for FeZSM-5 reported previously in the literature [38]. As noted earlier, the peak at 1.6 Å is assignable to backscattering from oxygen atoms coordinated to an iron absorber, whereas the assignment of the peak at 2.8 Å becomes complicated due to the contribution of Fe–Si and Fe–Al scatterings. Although the relative intensity of the second shell is much smaller than that for pure oxide, higher coordination spheres are clearly visible in the spectrum. On comparison of the χ functions shown in Fig. 5, it is found that a weak oscillation attributed to Fe–Fe scattering occurs at about 7.2 $Å^{-1}$ in *k* space, indicating the presence of Fe–Fe coordination shell for the Fe/HY-G*x* samples. It can be thus concluded that the peak at 2.8 Å in *R* space should be contributed mainly from Fe–Fe scattering.

The Fourier-filtered EXAFS data were fitted using a model consisting of a single Fe absorber coordinated to two shells of O atoms and one or two shells of Fe atoms. The best fits are shown in Fig. S1 (see Supplementary material) and fit results are given in Table 1 and point to the presence of oligonuclear clusters consisting of two or three iron atoms for the Fe/HY-G*x* samples. The sum of the O neighbors was found to be ca. 5. It was important to note that Fe/HY-G8.2, which contains Fe neighbor at distances similar to that

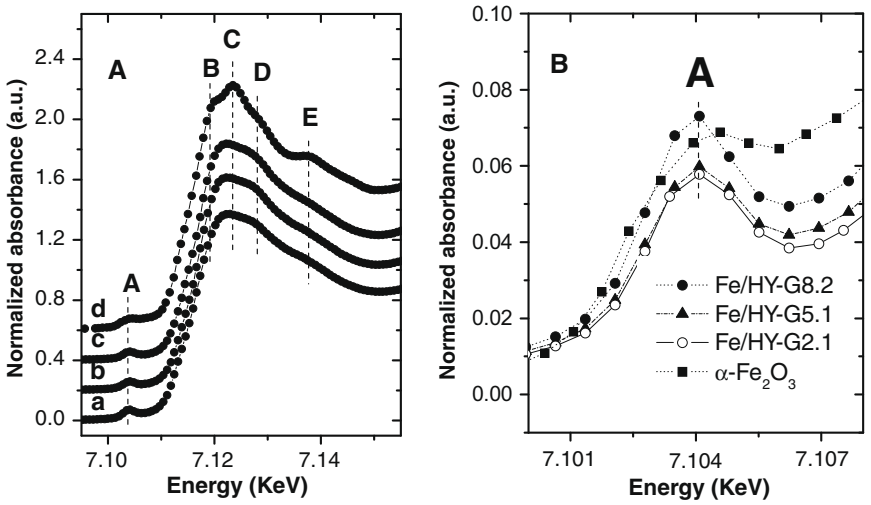

Fig. 4. (A) Normalized Fe K-edge XANES spectra of (a) Fe/HY-G8.2, (b) Fe/HY-G5.1, (c) Fe/HY-G2.1, and (d) α-Fe_2O_3. (B) The expanded view of the 1 s → 3 d pre-edge region. See text for details about A to E.

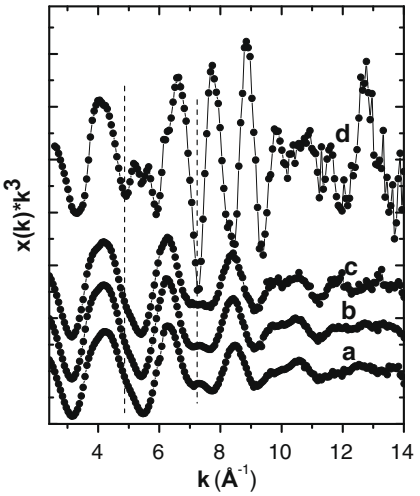

Fig. 5. The experimental K^3-weighted scattering functions of (a) Fe/HY-G8.2, (b) Fe/HY-G5.1, (c) Fe/HY-G2.1, and (d) α-Fe_2O_3.

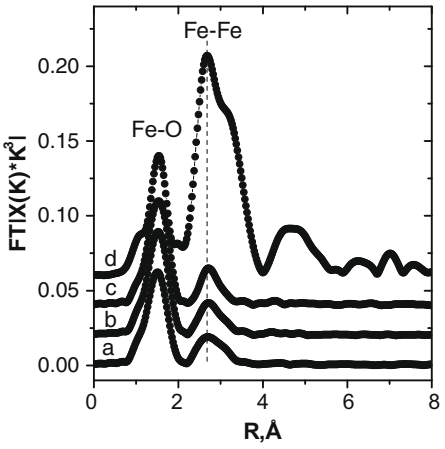

Fig. 6. Fourier transformations of K^3-weighted EXAFS spectra (uncorrected) of (a) Fe/HY-G8.2, (b) Fe/HY-G5.1, (c) Fe/HY-G2.1, and (d) α-Fe_2O_3 (K = 2.6 to 13.4 for α-Fe_2O_3; K = 2.4 to 14.2 for Fe/HY-Gx samples).

in α-Fe_2O_3, slightly differs from other two samples due to the higher content of iron. The fact that an additional Fe–Fe_2 shell is fitted at higher distances (R = 3.49 Å, CN = 0.2) is the result of further agglomeration of a minor fraction of iron. When the content of iron is controlled in the range of 2.1 to 5.1 wt.%, the Fe–Fe_2 shell is absent. We can thus exclude the presence of large Fe_2O_3 clusters. From the CN of the Fe–Fe shells, the Fe/HY-G2.1 sample represents the most binuclear clusters, estimated to account for ca. 100% of iron oligomers. With the increase in iron content, the content of binuclear clusters decreases slightly. Taking 15% error of CN into consideration, it is estimated that about 80% of iron oligomers is present in the binuclear state in the two Fe/HY-G5.1 and -G8.2 samples, and remnent 20% is iron oxide nanoclusters, or trinuclear clusters and isolated iron. It can be therefore concluded that a majority of iron species is presented as binuclear iron states in cavities of HY zeolite.

3.4. Electron paramagnetic resonance spectroscopy

Fig. 7 shows the EPR spectra recorded at 77 K of the Fe/HY-Gx (x = 2.1, 5.1, and 8.2) and Fe/HY-Ix (x = 5.0 and 2.0) samples. The EPR data of the Fe/HY-I2.0 and -I5.0 samples were used as a reference. Several signals can be distinguished at effective values of $g \approx 8.6$, 6.5, 4.3, 2.4, and 2.0. The assignment of such signals often detected in Fe-containing zeolites [5,17,18,21] is not straightforward. The number and position of observable EPR signals for Fe^{3+} species mainly depend on the local environment of these species and their possible magnetic interaction.

As proposed earlier for Fe-containing zeolites [39–41], the lines at $g \approx 4.3$ and $g \approx 8.6$ have been assigned to isolated Fe(III) ions in distorted tetrahedral coordination, and the weak signal at $g \approx 6.5$ can be attributed to isolated Fe^{3+} species in environments with more neighboring oxygen ions (5 or 6). Compared with the Fe/HY-I5.0 and -I2.0 samples, the three Fe/HY-Gx samples represent a lower intensity of the $g \approx 4.3$ EPR line, illuminating that the number of isolated tetrahedral iron in the Fe/HY-Gx samples is less than the two Fe/HY-I5.0 and -I2.0 samples. The distinct decrease in intensity of the $g \approx 4.3$ EPR line, with increasing iron content from (Fe/HY-G2.1) to (Fe/HY-G8.2), shows that the total amount of EPR-visible isolated Fe^{3+} decreases in the order of Fe/HY-G2.1 > Fe/HY-G5.1 > Fe/HY-G8.2. Especially, for the Fe/HY-G8.2 sample with the highest content of iron, isolated tetrahedral iron should be in a minor proportion, even negligible, as indicated by the nearly silent

Table 1
Fit results from EXAFS spectra reported in Fig. 6.

Sample	Shell	CN (15%)	R (Å) (10%)	$\Delta\sigma^2$ (Å^2) (10%)	ΔE_0 (eV) (10%)
α-Fe_2O_3	Fe–O	3.0	1.95	0.0024	17.9
	Fe–O	3.0	2.10	0.0043	10.3
	Fe–Fe_1	3.0	2.95	0.0039	13.8
	Fe–Fe_2	3.0	3.35	0.0041	6.29
	Fe–Fe_3	6.0	3.68	0.0081	10.5
Fe/HY-G8.2	Fe–O_1	3.0	1.93	0.0088	2.5
	Fe–O_2	1.8	2.01	0.0083	2.2
	Fe–Fe	1.3	3.08	0.010	8.0
	Fe–Fe	0.2	3.48	0.0031	8.1
Fe/HY-G5.1	Fe–O_1	3.0	1.93	0.0054	2.5
	Fe–O_2	1.7	2.05	0.0033	2.2
	Fe–Fe	1.5	3.11	0.010	8.5
Fe/HY-G2.1	Fe–O_1	3.0	1.94	0.0061	2.5
	Fe–O_2	1.8	2.04	0.0041	2.3
	Fe–Fe	1.0	3.11	0.0060	8.0

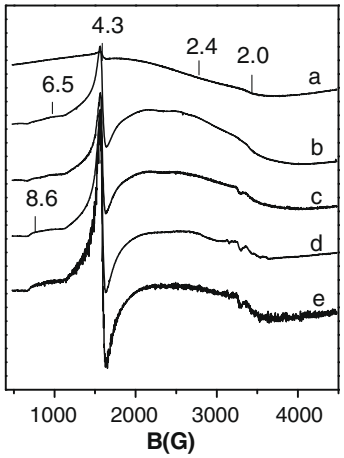

Fig. 7. EPR spectra recorded at 77 K of (a) Fe/HY-G8.2, (b) Fe/HY-G5.1, (c) Fe/HY-G2.1, (d) Fe/HY-I2.0, and (e) Fe/HY-I5.0.

EPR spectrum. It can be thus concluded that binuclear iron species, which are EPR silent, may be predominant in the Fe/HY-G8.2 sample as a consequence of the aggregation of isolated tetrahedral iron to form ESR-invisible nonparamagnetic oligonuclear iron species upon increasing the grafted amount of ferrocene.

These signals at the range of $2.6 \leqslant g \geqslant 2.0$ belong to superparamagnetic Fe oxide particles [40], whereas the assignment to the $g \approx 2.0$ EPR signal has been a matter of debate. It can arise either from isolated Fe^{3+} in high symmetry (D, $E \approx 0$) or from FeO_x oligomers in which magnetic interactions between the Fe^{3+} ions average out the zero field splitting, depending on its temperature dependence and line width. In the three Fe/HY-Gx samples, this signal decreases markedly in intensity with cooling to 77 K (the EPR data obtained at 298 K are not displayed in the present work), indicating that the line at $g \approx 2.0$ should be attributed to antiferromagnetic interaction between neighboring Fe^{3+} sites within clusters [40]. This further corroborates the above conclusion.

3.5. IR spectra of NO adsorption

To obtain further information on the coordination, isolation, and oxidation state of iron species in Y zeolite, Nitric oxide was used as a probe molecule to titrate surface iron sites. This method based on the exceptional affinity of NO towards Fe^{2+} centers has been already shown to be an informative and extremely sensitive technique designed to explore the structure and reactivity of surface sites [42]. Due to the presence of iron in +3 valence state in our samples as mentioned above, all samples were treated thermally in vacuum at 673 K for 3 h prior to introduction of NO so as to obtain Fe^{2+} ions.

Fig. 8 illustrates the evolution upon pressure (P_{NO}) of the FTIR spectra of NO adsorbed at room temperature on five Fe-containing Y zeolite samples. For three Fe/HY-Gx samples, a strong band at 1866 cm^{-1} with a weak shoulder at 1845 cm^{-1} and weak bands at 1918 and 1816 cm^{-1} are observed (Fig. 8A, B, and C). In contrast to Fe/HY-Gx, both Fe/HY-I5.0 and Fe/NaY-I5.0 show considerably different spectra of NO adsorption: a broad and weak band with some shoulders are observed on the Fe/NaY-I5.0, and the intensity of absorption bands observed on the Fe/HY-I5.0 is weaker than that on the Fe/HY-Gx. This indicates that there exists the remarkable difference in chemical states of iron species between the Fe/HY-Gx samples and the two samples prepared by the WI method. These two bands at 1866 and 1845 cm^{-1}, which are very similar to those observed for sublimed Fe/ZSM-5 and Fe/ZSM-5 prepared by solid-state ion exchange after oxidative pretreatment at 823 K, are ascribed to mono-nitrosyl coordinated to oligonuclear and isolated Fe^{2+} ions, respectively [22,43,44]. The pair of bands at 1918 and 1816 cm^{-1} is assigned to $Fe^{2+}(NO)_2$ [43,44]. The attribution of these bands to the same adsorbed species is confirmed by observing a straight line when the integrated area of the band at 1918 cm^{-1} is plotted versus that at 1816 cm^{-1} (see Supplementary material, Fig. S2).

Moreover, it is clearly observed that the intensities of these absorption bands in the nitrosyl region 1950 to 1700 cm^{-1} increase with increasing NO equilibrium pressure. For three Fe/HY-Gx (x = 8.2, 5.1, and 2.1) samples, the intensity of the main absorption peak at 1866 cm^{-1} is nearly unchanged upon increasing the NO pressure to 5.0 Torr, indicating that all of accessible Fe^{2+} sites are almost fully covered by NO. Whereas for Fe/HY-I5.0 and Fe/NaY-I5.0 (Fig. 8D and E), the NO adsorption can be nearly saturated at a lower NO equilibrium pressure (2.5 Torr). The NO adsorption amount is very low because a majority of iron species is presented as Fe_xO_y clusters and Fe_2O_3 nanoparticles. As for the Fe/HY-G5.1, Fe/HY-I5.0 and Fe/NaY-I5.0 samples with the almost same iron content, the intensity of the feature band of $Fe^{2+}NO$ at 1866 cm^{-1} is decreased in the order of Fe/HY-G5.1 $\gg$ Fe/HY-I5.0 > Fe/NaY-I5.0, suggesting that the Fe/HY-G5.1 sample contains more exposed oligonuclear Fe^{2+} ions after the thermal treatment under the same conditions. The result, in combination with the UV–vis DRS, and EXAFS results reported above, also indicates that the average nuclearity of iron in these three samples should increase in the order of Fe/HY-G5.1 < Fe/HY-I5.0 < Fe/NaY-I5.0.

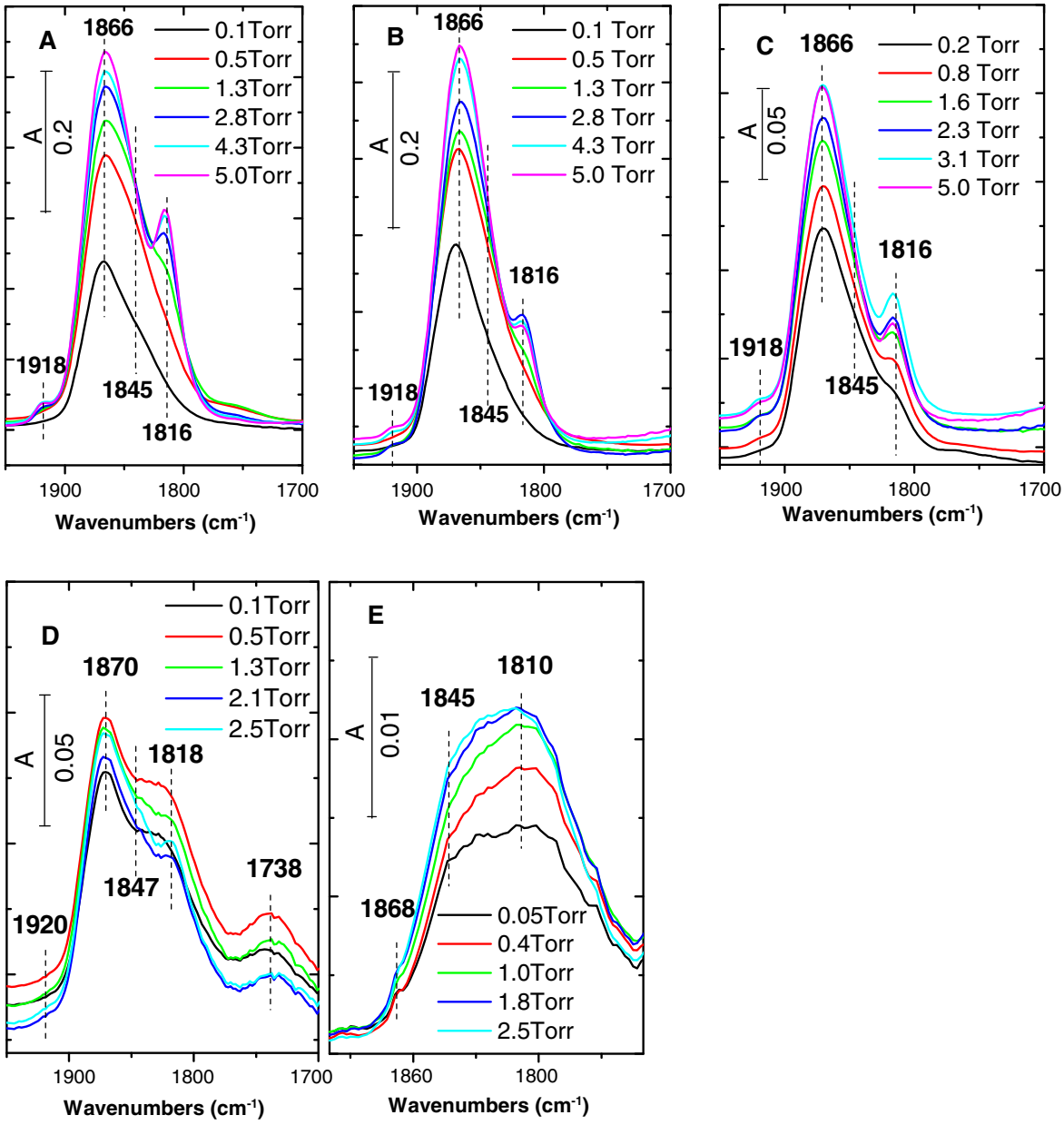

Fig. 8. FTIR spectra of NO adsorbed at room temperature on (A) Fe/HY-G8.2, (B) Fe/HY-G5.1, (C) Fe/HY-G2.1, (D) Fe/HY-I5.0, and (E) Fe/NaY-I5.0.

3.6. Catalytic activity

It can be predicted that the difference between iron species of the three Fe/HY-G*x* samples and the Fe/HY-I5.0 and Fe/NaY-I5.0 samples will result in different catalytic behaviors. In this study, phenol hydroxylation with H_2O_2 as oxidant was used as a model reaction to examine the catalytic properties of the Fe/HY-G*x*, Fe/HY-I5.0, Fe/NaY-I5.0, and nano-α-Fe_2O_3 samples. Before comparison of these catalysts, we examine emphatically the effect of reaction parameters, such as reaction temperature and H_2O_2/phenol molar ratio, in order to optimize the reaction conditions and to better understand the nature of iron-catalyzed phenol reaction. The Fe/HY-G8.2 sample was used as a representative catalyst to study these factors.

The effects of temperature and H_2O_2/phenol molar ratio on phenol hydroxylation in water are shown in Figs. 9 and 10, respectively. The reaction proceeds rapidly and reaches a final state within 5 to 10 min after a short induction time. The reaction stops at incomplete phenol conversion due to the unproductive decomposition of H_2O_2. Similar observation was reported for other Fe-containing catalysts [16,45]. Higher reaction temperature (330 K) can accelerate the emergence of hydroxylation reaction. More pronounced induction period is observed at lower reaction temperature (320 K) and at lower H_2O_2/phenol ratios (0.5 and 0.7), but temperature does not affect the final phenol conversion, which is governed by H_2O_2/phenol molar ratio, as shown in Fig. 10. The phenol conversion increases prominently from ca. 30% to ca. 75% with increasing H_2O_2/phenol molar ratio from 0.5 to 2.0. It is unexpected that a higher H_2O_2/phenol molar ratio (2.0) does not further shorten the induction period, suggesting that H_2O_2/phenol ratio is not the natural factor affecting induction period. Considering the phenol conversion and induction time, the H_2O_2/phenol molar ratio of 1:1 and the reaction temperature of 330 K should be two optimum parameters.

The catalytic activities of all samples for phenol hydroxylation under the standard set of experimental conditions (phenol:H_2O_2 = 1:1, water solvent, catalyst: 50 mg, temperature: 330 K) are shown

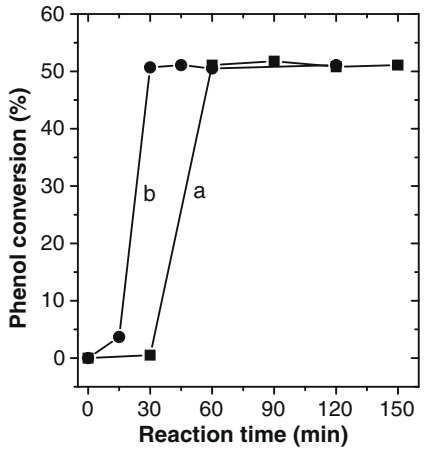

Fig. 9. Phenol conversion profiles obtained at different temperatures (a: 320 K, b: 330 K) and phenol: H_2O_2 = 1:1 in water using Fe/HY-G8.2 catalyst.

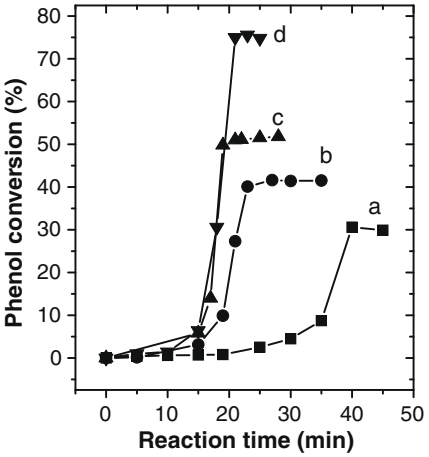

Fig. 10. Phenol conversion profiles obtained at 330 K and different phenol/H_2O_2 ratios in water using Fe/HY-G8.2 catalyst: (a) phenol: H_2O_2 = 2:1; (b) phenol: H_2O_2 = 1:0.7; (c) phenol: H_2O_2 = 1:1; (d) phenol: H_2O_2 = 1:2.

in Fig. 11 and summarized in Table 2, where catechol, hydroquinone, and *para*-benzoquinone are main products formed catalytically in liquid phase. The three Fe/HY-G*x* catalysts represent the same phenol conversion (ca. 51%) at 330 K, evidently higher than Fe/HY-I5.0 (48%), Fe/NaY-I5.0 (43.2%), and nano-α-Fe_2O_3 (43.2%), whereas all Fe/HY catalysts including the nano-α-Fe_2O_3 exhibit the comparable selectivity to products, irrespective of the iron content and the preparation method of samples.

Interestingly, a notable difference in the induction period of reaction is observed for these catalysts. Induction time for the three Fe/HY-G*x* samples decreases with increasing iron content. It demonstrates that there exists an inherent relationship between the induction period and the iron content. But by comparison with the Fe/HY-G5.1, both Fe/HY-I5.0 and Fe/NaY-I5.0 with the same iron content show a longer induction period, as seen in Fig. 11. This shows that the iron-catalyzed phenol hydroxylation is more dependent on the chemical states of iron in cavities of Y zeolite, which will be discussed below in combination with the characterization results.

4. Discussion

4.1. Local structure of binuclear iron species

According to the results reported above, it can be concluded that Fe species in three Fe/HY zeolites prepared by the SOMC method have a high dispersity and a low nuclearity in the range from monomer to trimer or tetramer. Despite the three samples having the broad iron content in the range of 2.1 to 8.2 wt.% as shown by element analysis, they represent the similar UV–vis, IR, EPR, and EXAFS spectra. Analysis of the EXAFS spectra demonstrated the presence of diferric binuclear clusters as the predominant form of iron in the Fe/HY-G2.1 and -G5.1 samples and the absence of Fe_2O_3 clusters. Of course, isolated iron and trinuclear iron visible in EPR spectrum accounts for a certain percentage of total Fe present in the Fe/HY-G2.1and -G5.1 samples based on the EPR results. With increasing iron content to 8.2 wt.%, iron oxide clusters with a high nuclearity are observed by UV–vis spectroscopy. But the fitting results of the EXAFS data of Fe/HY-G8.2 show a Fe–Fe_1 CN of 1.3 and an additional shell (Fe–Fe_2, 3.49 Å) with a low CN (0.2) that had to be introduced for optimizing the fitting of the Fe–Fe scattering, indicating that the agglomeration phenomena involved only a minor fraction of iron (below 10%). The majority of Fe species is present in the diferric binuclear state.

Based on the EXAFS fitting results, presumably, there are four kinds of possible structures for the diferric binuclear species, as depicted in Fig. 12. The structural models a, b, and c have already been suggested in Fe/ZSM-5 prepared by CVD or solid-state ion exchange of $FeCl_3$. Marturano et al. [23] thought that diferric binuclear clusters consist of a diamond core similar to that of the monooxygenase enzyme (MMOH) on the basis of the EXAFS results, as depicted in Fig. 12a and b. Battiston et al. [24] studied in detail the effect of post-treatment on the structure and reactivity of the Fe-binuclear complexes in over-changed Fe/ZSM-5 by in situ EXAFS spectroscopy. They found that above 250 °C in He a significant fraction of iron undergoes auto-reduction accompanied by the removal of approximately one oxygen atom from the closest Fe–O_1 shells ascribable to Fe–O–Fe bridging oxygen atom. According to the findings, the authors suggested that the diferric binuclear complex in mildly calcined Fe/ZSM-5 can be described with a $Fe^{III}_2(\mu\text{-O})_2$ core, as depicted in Fig. 12c. The Fe–Fe_1 distance of 3.08 to 3.11 Å and the Fe–O_2 distance of 2.01 to 2.05 Å for the three Fe/HY-G*x* samples are clearly longer than those in the model c (Fe–Fe: 3.0 Å, Fe–O_1: 1.86 Å), and yet are in good agreement with the Fe–Fe and Fe–O distances obtained for the $Fe^{III}_2(\mu\text{-OH})_2$ core (Fe–Fe: 3.08 to 3.16 Å; Fe–O: 1.96 to 2.02 Å) [46–48]. It seems that diferric binuclear species in these three Fe/HY-G*x* samples should contain one or two μ-hydroxo bridges similar to the models a and b. But one distinct difference is that the Fe–O_3 shell at ca. 2.5 Å in the models a and b is not observed for our samples. If the Fe–O_3 shell at ca. 2.5 Å is considered to fit our EXAFS data, a poor fit can be obtained. It is evident that diferric binuclear species with the structural model a or b or c do not exist in our Fe/HY-G*x* samples. The Fe–O_1 distance of 1.93 to 1.95 Å is in good agreement with the average distance found for Fe–O–Al bridging oxygen [19,24,30]. Significantly shorter Fe–O distances are nevertheless reported in the literature for Fe–O–Fe oxo-bridges (1.82 to 1.88 Å) [23–25,49], and thus we can ascribe oxygen located in shell Fe–O_1 to bridging (Fe–O–Al) atom, by which the iron atoms are stabilized to the zeolite lattice. The observed Fe–O_2 distance of 2.01 to 2.05 Å is not only consistent with the Fe–O distance obtained for the $Fe^{III}_2(\mu\text{-OH})_2$ core (1.96 to 2.02 Å) as above-described, but also in good agreement with quantum chemical calculations of Fe cation associated with two OH groups [50]. On the basis of the above analysis, we can give a structural model of the binuclear [Fe^{III}–(μ-O)(μ-OH)–Fe^{III}] as depicted in Fig. 12d.

The model can well explain two experiment results obtained in this work. One is auto-reduction of Fe^{3+}, which likewise takes place on our Fe/HY-G*x* samples. Thermal treatment in vacuum at 673 K makes a majority of Fe^{3+} ions of diferric binuclear species reduce to Fe^{2+} ions, which are titrated by adsorbing NO molecule to form $Fe^{2+}(NO)_n$ complexes as characterized by extremely intense ν(NO)

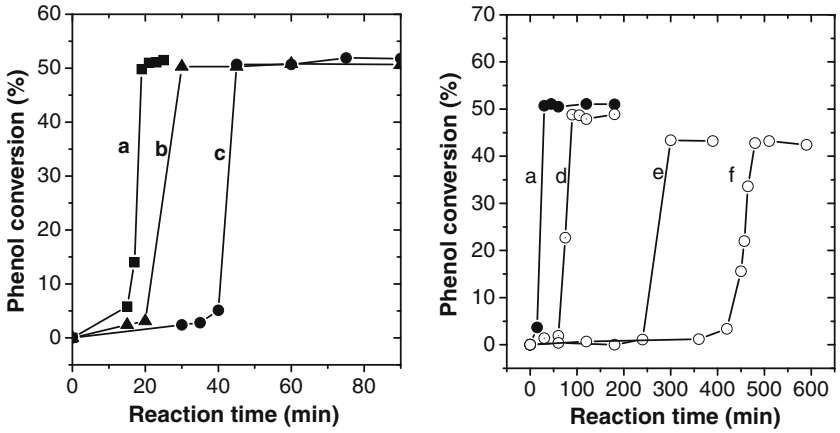

Fig. 11. Comparison of phenol conversion profiles obtained at 330 K and phenol:H_2O_2 = 1:1 in water using different Fe-containing catalysts: (a) Fe/HY-G8.2, (b) Fe/HY-G5.1, (c) Fe/HY-G2.1, (d) Fe/HY-I5.0, (e) Fe/NaY-I5.0, and (f) Nano-α-Fe_2O_3.

Table 2
Catalytic performances of the Fe/HY-G*x* samples for the hydroxylation of phenol.

Sample	Preparation method	Iron content (wt.%)	X_{phenol} (mol%)[a]	Product distribution (mol%)			S_{hydrox} (mol%)[c]
				S_{CAT}[b]	S_{HQ}	S_{BQ}	
No catalyst	–	–	0.0	–	–	–	–
Fe/HY-G8.2	SOMC	8.2	51.1	38.3	30.3	1.1	68.6
Fe/HY-G5.1	SOMC	5.1	51.5	37.4	29.0	1.2	66.4
Fe/HY-G2.1	SOMC	2.1	51.2	38.7	28.1	1.4	66.8
Fe/HY-I5.0	WI	5.0	48.0	39.9	29.1	1.2	70.0
Fe/NaY-I5.0	WI	5.0	43.2	37.6	29.8	1.7	67.4
Nano-α-Fe_2O_3		100	43.2	39.6	27.6	1.6	67.2

Reaction conditions: amount of catalyst = 50 mg; volume of solvent (H_2O) = 20 ml; H_2O_2/phenol = 1:1 (mol/mol); temperature = 330 K; reaction time: 1 h for the Fe/HY-G*x* and Fe/HY-I5.0 samples; 5 h for the Fe/NaY-I5.0 sample; 8 h for the Nano-α-Fe_2O_3 sample.

[a] X_{phenol} (%) is the conversion of phenol, X_{phenol} (%) = 1 − molar concentration of phenol after sampling/molar concentration of phenol before reaction.

[b] CAT is catechol, HQ is hydroquinone, BQ is *para*-benzoquinone, S_{CAT} (%) = molar concentration of CAT after reaction/molar concentration of phenol (before reaction − after reaction); which is similar to S_{HQ} and S_{BQ}.

[c] $S_{hydrox} = S_{CAT} + S_{HQ}$.

IR bands shown in Fig. 8. Recently, Guesmi et al. [51] proposed that the auto-reduction proceeds by a dehydroxylation pathway instead of oxygen removal and justified the formation of the active site [Fe^{II}-(μ-OH)-Fe^{II}] using the density functional theory (DFT). Considering the lack of the removable bridging oxygen in the model d, the auto-reduction appearing at our Fe/HY-G*x* samples should follow the proposed dehydroxylation pathway. Another is the Fe-OH groups. Although the Fe-OH groups could be removed upon thermal treatment in vacuum at 673 K, such a treatment cannot lead to the reduction of all binuclear diferric centers to [Fe^{II}–(μ-OH)–Fe^{II}]. Thus, we can observe the IR absorption band at 3687 cm^{-1} belonging to Fe^{III}–OH groups after thermal treatment in vacuum as shown in Fig. 2.

As for the formation of the binuclear diiron species, the most important factor is calcination at high temperature, which often makes Fe-oxo species in zeolites aggregated to oligomers and even to small Fe_2O_3 particles, leading to the coexistence of isolated Fe-oxo species, Fe_xO_y oligomers, and small Fe_2O_3 particles. The degree of the thermal aggregation is generally dependent on post-treatment conditions and preparation methods. Especially in the presence of water vapor, the aggregation of iron entities into larger oligomers becomes more extensive. However, for the Fe/HY-G*x* samples prepared by the SOMC method based on analogous intermolecular reaction [29], the majority of iron species is presented as binuclear states. Iron oxide particles are not formed upon calcination at 773 K for 6 h in air, indicating that the aggregation of iron ions is very gentle. One main origin is that the iron derived from mononuclear cyclopentadiene–iron complexes was isolated and homogeneously distributed in cavities of zeolite prior to calcination. The iron atom of cyclopentadiene iron complex was coordinated, on average, to three oxygen atoms of the zeolite surface with a Fe–O distance of 2.00 Å [29]. The strong bonding to bridging oxygen atoms of zeolite framework inhibits the iron migration during calcination to a certain extent. Our previous study showed that the majority of iron-grafted in supercages of HY zeolite is present in isolated tetrahedral coordination with the Fe–O_1 distance of ca. 1.94 Å when the iron content is below 1.4% [30]. In this study, we achieve a controllable synthesis of binuclear diiron species by varying the grafted amount of ferrocene into cavities of HY zeolite. The increase in iron content is indeed also an important factor to the formation of binuclear iron species. One therefore thinks that the surface organometallic chemistry of ferrocene is an alternative route to construct diferric binuclear active sites in cavities of zeolites besides the CVD of $FeCl_3$.

4.2. Nature of iron-catalyzed phenol hydroxylation

The catalytic phenol hydroxylation with H_2O_2 as oxidant has been known to proceed via a free-radical reaction mechanism. Free-radical may be generated on the solid catalyst surface in two ways as illustrated in Scheme 1: (1) the catalyst accelerates the decomposition of H_2O_2 into hydroxyl radicals (Eqs. (1) and (2)), [52] or (2) the catalyst activates the phenol molecules directly, and facilitates the formation of phenoxy radicals (Eqs. (3) and (4)) [45]. To explore which way is possible in phenol hydroxylation catalyzed by Fe-based catalysts, we monitor the yields of catechol,

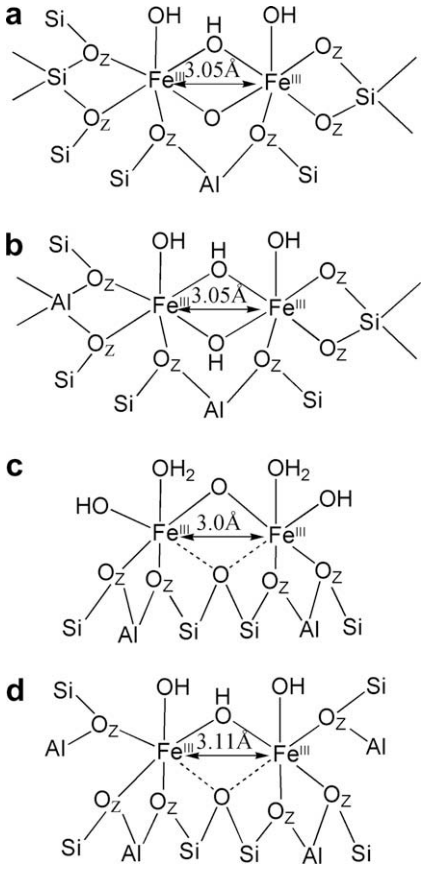

Fig. 12. Structure of binuclear Fe complexes reported in the literatures (a, b) [23] and (c) [24]; (d) Proposed local structure of binuclear iron species in Fe/HY-G*x* samples prepared by surface organometallic chemistry of ferrocene.

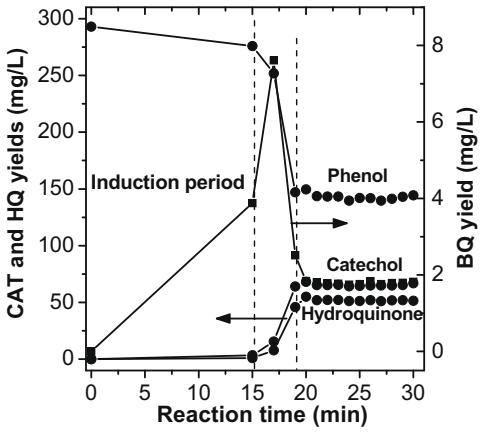

Fig. 13. The yields of catechol, hydroquinone, and *para*-benzoquinone obtained using Fe/HY-G8.2 catalyst as function of time-on-stream.

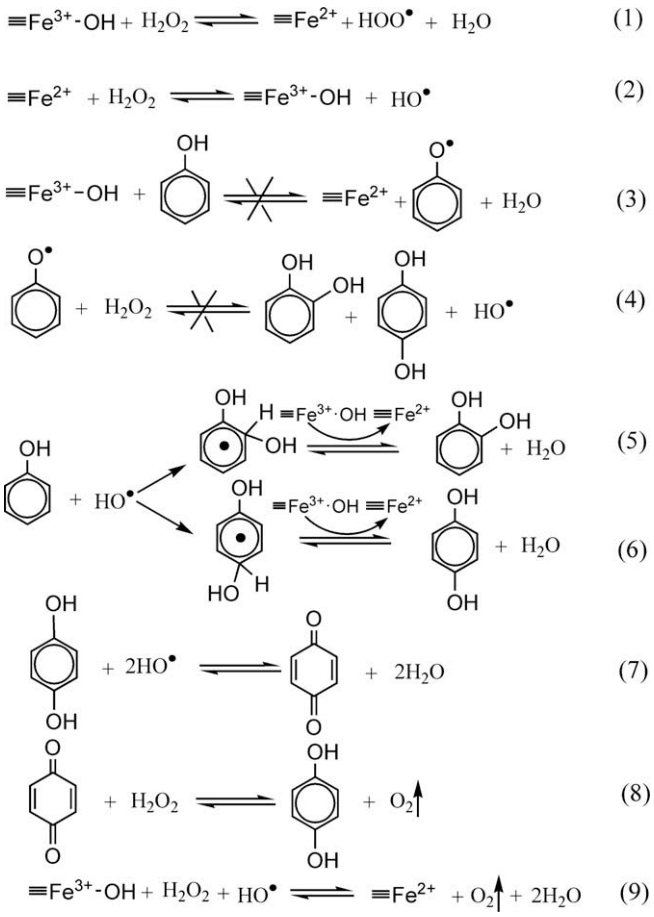

Scheme 1. Reaction pathway of iron-catalyzed phenol hydroxylation [16,52].

hydroquinone, and *para*-benzoquinone as function of time-on-stream, as shown in Fig. 13. Within induction period, neither catechol nor hydroquinone is detected and *para*-benzoquinone increases gradually in concentration with decrease of phenol, indicating that iron-catalyzed phenol hydroxylation is not initiated by phenoxy radicals, but initiated by hydroxyl radicals produced by the decomposition of H_2O_2 over active iron sites. A minor fraction of phenol is oxidized to *para*-benzoquinone by O_2 generated from the unproductive decomposition of H_2O_2. After induction period, hydroxylation reaction proceeds quickly. Both Catechol and hydroquinone are produced and rapidly increase in concentration with sharp decrease of phenol (Eqs. (5) and (6)). The origin of the sudden speedup of the reaction remains unclear. It may be originated from a certain intermediate formed, which also takes part in the decomposition of H_2O_2 to HO. It is important to note that the yield of *para*-benzoquinone reaches a maximum at initial stage of the hydroxylation reaction, followed by a sharp decrease. The same phenomenon is observed using α-Fe_2O_3 as catalyst for phenol hydroxylation (see Fig. S3 in Supplementary material), suggesting that *para*-benzoquinone is a very important reactive intermediate formed in phenol hydroxylation. Its role in the reaction needs to be further studied. The formation of *para*-benzoquinone originates mainly from a fast oxidization of hydroquinone after induction period (Eq. (7)). The subsequent disappearance maybe results from the transformation of para-benzoquinone into hydroquinone (Eq. (8)) and the deep oxidation of para-benzoquinone, at least in large part, to black tarry material. The hydroxyl radical mechanism proposed above (Scheme 1) can well explain the iron-catalyzed phenol hydroxylation behavior.

It is evident that the decomposition of H_2O_2 to hydroxyl radical is the rate-determining step of the iron-catalyzed phenol hydroxylation. The mechanism of the catalytic decomposition of H_2O_2 over iron oxides has been described in the literature [53]. The initiation reaction involves the reduction of Fe^{3+} and the oxidation of Fe^{2+} resulting in the formation of hydroxyl radical, as presented in Eqs. (1) and (2). When the proper amount of HO was produced, the hydroxylation of phenol could be initiated (Eqs. (5) and (6)). The activity results reported above indicate that the final conversion of phenol is dominated by the H_2O_2/phenol molar ratio. It

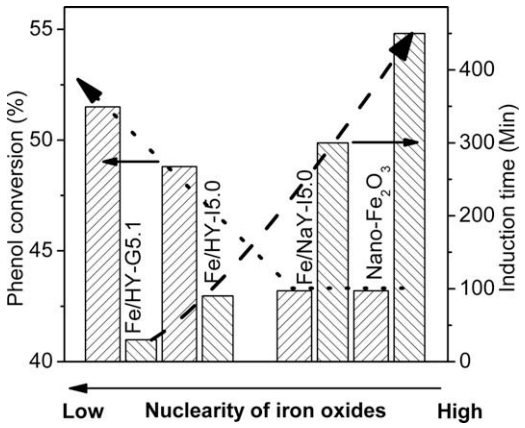

Fig. 14. Relationship between phenol conversion and nuclearity of iron-oxo species.

appears to be independent of the number of active iron sites due to the lack of change in phenol conversion of the three Fe/HY-G*x* samples with 2.1 to 8.2 wt.% of iron content. Whereas the increase of active iron sites can enhance the decomposition rate of H_2O_2 into hydroxyl radicals, and consequently shorten induction period. The induction period and the conversion of phenol in iron-catalyzed phenol hydroxylation are related with the average nuclearity of iron species in zeolites, as shown in Fig. 14. Both iron oxide nanoclusters occlude in cavities of zeolite (Fe/NaY-I5.0) and iron oxide nanoparticles (Nano-α-Fe_2O_3) exhibit a lower conversion of phenol compared to Fe/HY-G*x* and Fe/HY-I5.0. The lower conversion of phenol is originated from the ineffective consumption of a fraction of H_2O_2 within a long induction period. Obviously, the formation of appropriate amount of active Fe(III) sites on the catalyst surface is a key to initiating the phenol hydroxylation, but it needs long time for α-Fe_2O_3 since hematite α-Fe_2O_3 was reported to be an inefficient catalyst for the decomposition rate of H_2O_2 compared to ferrihydrite and goethite [54], as seen in Fig. 9. The phenol hydroxylation over α-Fe_2O_3 is subjected to a long induction period. Isolated or oligonuclear iron species with low nuclearity in cavities of HY zeolite facilitate the quick decomposition of H_2O_2 into hydroxyl radicals, giving rise to a shorter induction period and a higher conversion of phenol. The IR characterization results indicate that the content of isolated and binuclear iron species decreases in the order Fe/HY-G5.1 > Fe/HY-I5.0 > Fe/NaY-I5.0. Such a decrease in content of isolated and binuclear iron species results in a corresponding increase in induction time in the order Fe/HY-G5.1 < Fe/HY-I5.0 < Fe/NaY-I5.0, as shown in Fig. 14. It shows that isolated and oligonuclear iron species with low nuclearity in cavities of Y Zeolite should be the active sites for phenol hydroxylation.

5. Conclusions

Introduction of ferrocene in HY zeolite by sublimation and subsequent removal of one cyclopentadienyl ligand results in the attachment of Fe atom to O_1 sites framework that lie approximately in a plane of a 12-membered ring connecting the supercages. The grafted amount of ferrocene considerably affects the final states of iron. The analysis of the EXAFS data shows that the majority of iron in three Fe-grafted HY zeolites with iron content in the range of 2.1 to 8.2 wt.%, obtained by the surface organometallic chemistry of ferrocene and subsequent calcination in air, consists of hydroxo-bridged binuclear Fe complexes with a [HO–Fe^{III}–(μ-OH)–Fe^{III}–OH] core. IR spectra of NO adsorbed reveal that the majority of the binuclear diferric species is subjected to auto-reduction upon thermal treatment in vacuum at 673 K, and consequently can be titrated by NO.

The chemical states of iron in Fe/HY and Fe/NaY with iron content of 5.0 wt.%, prepared by the WI method, were also investigated by means of UV–vis DRS and NO adsorption IR spectroscopies in order to compare with the iron-grafted HY zeolite with the almost same iron content (5.1 wt.%). UV–vis absorption and IR results clearly indicate that Fe is hosted on the three zeolites in different forms. In the case of Fe/HY-I5.0, Fe was presented as a complex mixture of iron sites from isolated iron cations to oxidic clusters. Fe in Fe/HY-G5.1 was found in the predominant form of the diferric binuclear clusters, whereas iron oxide nanoclusters were predominant in Fe/NaY-I5.0. The chemical states of iron ion in cavities of Y zeolite strongly influence the catalytic activity for phenol hydroxylation with H_2O_2 as oxidant. The three iron-grafted HY zeolites presented a stable activity irrespective of iron content and a short induction period, whereas both Fe/HY-I5.0 and Fe/NaY-I5.0 showed a decreasing phenol conversion and a long induction period. The combined characterization results show that both phenol conversion and induction time are related to the nuclearity of iron oxide species. The decrease in nuclearity of iron oxides from nanoparticles to dinuclear hydroxo-bridged iron clusters can lead to the increase of phenol conversion and the drastic decrease in induction time, as a consequence of the rapid decomposition of H_2O_2 over the dinuclear iron clusters into hydroxyl radical. It is therefore suggested that the active sites are isolated and oligonuclear iron centers with low nuclearity.

In summary, this study demonstrates a general picture that diferric binuclear active sites can be constructed easily, in a reproducible manner, in cavities of zeolites by surface organometallic chemistry of ferrocene instead of the CVD of $FeCl_3$, and gains a deeper understanding of the nature of iron-catalyzed phenol hydroxylation.

Acknowledgments

This work was financially supported by the National Natural Science Foundation of China (grant Nos. 20673020 and 20537010), National Basic Research Program of China (973 Program, No. 2007CB613306), the National High Tech R&D Program of China (863 Program, 2008AA06Z326), and program for New Century Excellent Talents in University (XSJRC2007-19), Fujian Province of PR China. The authors thank Professor Yaning Xie, Beijing Photo Factory for the XAFS experiment and the reviewers' helpful discussion.

Appendix A. Supplementary material

Supplementary data associated with this article can be found, in the online version, at doi:10.1016/j.jcat.2009.04.002.

References

[1] W.M.H. Sachtler, Acc. Chem. Res. 26 (1993) 383.
[2] W.M.H. Sachtler, in: B. Zhou, S. Han, R. Raja, G.A. Somorjai (Eds.), Nanotechnology in Catalysis, Springer, New York, 2007, p. 139.
[3] B.C. Gates, Chem. Rev. 95 (1995) 511.
[4] E. Berrier, O. Ovsitser, E.V. Kondratenko, M. Schwidder, W. Grünert, A. Brückner, J. Catal. 249 (2007) 67.
[5] B.R. Wood, J.A. Reimer, A.T. Bell, M.T. Janicke, K.C. Ott, J. Catal. 224 (2004) 148.
[6] J.A.Z. Pieterse, S. Booneveld, R.W. van den Brink, Appl. Catal. B: Environ. 51 (2004) 215.
[7] M. Schwidder, M.S. Kumar, K. Klementiev, M.M. Pohl, A. Brückner, W. Grünert, J. Catal. 231 (2005) 314.
[8] M. Iwasaki, K. Yamazaki, K. Banno, H. Shinjoh, J. Catal. 260 (2008) 205.
[9] F. Heinrich, C. Schmidt, E. Löffler, M. Menzel, W. Grünert, J. Catal. 212 (2002) 157.
[10] G.I. Panov, CATTECH 4 (2000) 18.

[11] A. Ribera, I.W.C.E. Arends, S.D. Vries, J. Pérez-Ramírez, R.A. Sheldon, J. Catal. 195 (2000) 287.
[12] H.-Y. Chen, W.M.H. Sachtler, Catal. Today 42 (1998) 73.
[13] Q. Zhang, Q. Guo, X. Wang, T. Shishido, Y. Wang, J. Catal. 239 (2006) 105.
[14] H. Xin, J. Liu, F. Fan, Z. Feng, G. Jia, Q. Yang, C. Li, Micrcopor. Mesopor. Mater. 113 (2008) 231.
[15] A.L. Villa, C.A. Caro, C.M. de Correa, J. Mol. Catal. A: Chem. 228 (2005) 233.
[16] J.-S. Choi, S.-S. Yoon, S.-H. Jang, W.-S. Ahn, Catal. Today 111 (2006) 280.
[17] P. Fejes, K. Lázár, I. Marsi, A. Rockenbauer, L. Korecz, J.B. Nagy, S. Perathoner, G. Centi, Appl. Catal. A: Gen. 252 (2003) 75.
[18] G. Berlier, G. Spoto, G. Ricchiardi, P. Fisicaro, A. Zecchina, I. Rossetti, E. Selli, L. Forni, E. Giamello, C. Lamberti, J. Catal. 208 (2002) 64.
[19] A.A. Battiston, J.H. Bitter, F.M.F. de Groot, A.R. Overweg, O. Stephan, J.A. van Bokhoven, P.J. Kooyman, C. van der Spek, G. Vankó, D.C. Koningsberger, J. Catal. 213 (2003) 251.
[20] S. Bordiga, R. Buzzoni, F. Geobaldo, C. Lamberti, E. Giamello, A. Zecchina, G. Leofanti, G. Petrini, G. Tozzola, G. Vlaic, J. Catal. 158 (1996) 486.
[21] M.S. Kumar, M. Schwidder, W. Grünert, A. Brückner, J. Catal. 227 (2004) 384.
[22] L.J. Lobree, I.-C. Hwang, J.A. Reimer, A.T. Bell, J. Catal. 186 (1999) 242.
[23] P. Marturano, L. Drozdová, A. Kogelbauer, R. Prins, J. Catal. 192 (2000) 236.
[24] A.A. Battiston, J.H. Bitter, W.M. Heijboer, F.M.F. de Groot, D.C. Koningsberger, J. Catal. 215 (2003) 279.
[25] J. Jia, K.S. Pillai, W.M.H. Sachtler, J. Catal. 221 (2004) 119.
[26] I. Yuranvo, D.A. Bulushev, A. Renken, L. Kiwi-Minsker, J. Catal. 227 (2004) 138.
[27] K. Sun, H. Xia, Z. Feng, R. van Santen, E. Hensen, C. Li, J. Catal. 254 (2008) 383.
[28] M.H. Baik, M. Newcomb, R.A. Friesner, S.J. Lippard, Chem. Rev. 103 (2003) 2385.
[29] J. Long, X. Wang, G. Zhang, J. Dong, T. Yan, Z. Li, X. Fu, Chem. Eur. J. 13 (2007) 7890.
[30] X. Wang, J. Long, G. Yan, G. Zhang, X. Fu, J.-M. Basset, F. Lefebvre, Micropor. Mesopor. Mater. 108 (2008) 258.
[31] F.R. Sarria, O. Marie, J. Saussey, M. Daturi, J. Phys. Chem. B 109 (2005) 1660.
[32] J. Long, X. Wang, Z. Ding, L. Xie, Z. Zhang, J. Dong, H. Lin, X. Fu, J. Catal. 255 (2008) 48.
[33] I. Kiricsi, C. Flego, G. Pazzuconi, W.O. Parker, R. Millini Jr., C. Pergo, G. Bellussi, J. Phys. Chem. 98 (1994) 4627.
[34] T. Nobukawa, M. Yoshida, S. Kameoka, S.I. Ito, K. Tomishige, K. Kunimori, J. Phys. Chem. B 108 (2004) 4071.
[35] T. Ishikawa, S. Nitta, S. Kondo, J. Chem. Soc., Faraday Trans. 1 (82) (1986) 2401.
[36] G.D. Pringruber, P.K. Roy, R. Prins, Phys. Chem. Chem. Phys. 8 (2006) 3939.
[37] G. Yan, J. Long, X. Wang, Z. Li, X. Wang, Y. Xu, X. Fu, J. Phys. Chem. C 111 (2007) 5195.
[38] S.H. Choi, B.R. Wood, J.A. Ryder, A.T. Bell, J. Phys. Chem. B 107 (2003) 11843.
[39] A.V. Kucherov, M. Shelef, J. Catal. 195 (2000) 106.
[40] E.A. Zhilinskaya, G. Delahay, M. Mauvezin, B. Coq, A. Aboukais, Langmuir 19 (2003) 3596.
[41] S. Faggian, P. Fisicaro, E. Giamello, R. Gobetto, A. Viale, G. Berlier, C. Lamberti, I. Rossetti, J. Phys. Chem. B 107 (2003) 8922.
[42] A. Zecchina, M. Rivallan, G. Berlier, C. Lamberti, G. Ricchiardi, Phys. Chem. Chem. Phys. 9 (2007) 3483.
[43] R.W. Joyer, M. Stockenhuber, J. Phys. Chem. B 103 (1999) 5963.
[44] G. Mul, M.W. Zandbergen, F. Kapteijn, J.A. Moulijn, J. Pérez-Ramírez, Catal. Lett. 93 (2004) 113.
[45] C. Xiong, Q. Chen, W. Lu, H. Gao, W. Lu, Z. Gao, Catal. Lett. 69 (2000) 231.
[46] C.C. Ou, R.A. Lalancette, J.A. Potenza, H.J. Schugar, J. Am. Chem. Soc. 100 (1978) 2053.
[47] J.A. Thich, C.C. Ou, D. Powers, B. Vasilion, D. Mastropaolo, J.A. Potenza, H.J. Schugar, J. Am. Chem. Soc. 98 (1976) 1425.
[48] L. Borer, L. Thalken, C. Ceccarelli, M. Glick, J.H. Zhang, W.M. Reiff, Inorg. Chem. 22 (1983) 1719.
[49] H.F. Hsu, Y. Dong, L. Shu, V.G.J. Young, L.J. Que, J. Am. Chem. Soc. 121 (1999) 5230.
[50] S.H. Choi, B.R. Wood, A.T. Bell, M.T. Janicke, K.C. Ott, J. Phys. Chem. B 107 (2004) 8970.
[51] H. Guesmi, D. Berthomieu, L. Kiwi-Minsker, J. Phys. Chem. C 112 (2008) 20319.
[52] C. Liu, Y. Shan, X. Yang, X. Ye, Y. Wu, J. Catal. 168 (1997) 35.
[53] S.S. Lin, M.D. Gurol, Environ. Sci. Technol. 32 (1998) 1417.
[54] H.H. Huang, M.C. Lu, J.N. Chen, Water. Resour. 35 (2001) 2291.